***Journal of Global Positioning Systems* (*2021*)**
Vol. 17, No. 1: 15-33
DOI: 10.5081/jgps.17.1.15

Improvement of Integrated Water Vapor Products from Sentinel-3 OLCI NIR Channels Using Ground-based GPS Measurements

Jiafei Xu and Zhizhao Liu*

Department of Land Surveying and Geo-Informatics and Research Institute for Sustainable Urban Development, Hong Kong Polytechnic University, Hong Kong

E-mail: 20074506r@connect.polyu.hk; lszzliu@polyu.edu.hk

* *Corresponding author*

***Abstract*—**High-quality remote sensing water vapor monitoring plays a vital role in Earth's weather and climate observation. In this work, we developed a model to improve the accuracy of integrated water vapor (IWV) products retrieved from the Ocean and Land Color Instrument (OLCI) near-infrared (NIR) channels using ground-based GPS-derived IWV data. This algorithm uses the empirical regression equations to calibrate the official OLCI IWV products published by Sentinel-3. The reference IWV data, from June 1, 2018 to May 31, 2019, from 453 GPS sites over Australia, were employed to calculate the differential IWV data by subtracting GPS IWV data from OLCI IWV data. The OLCI IWV pixels were grouped into two categories according to the quality flag of each pixel. For each group, the relationship between the differential IWV data and the official OLCI IWV products was defined, and the model parameters were independently calculated from each season. The performance of the model was evaluated using reference IWV data from GPS and European Centre for Medium-Range Weather Forecasts (ECMWF) from June 1, 2019 to May 31, 2020 over Australia. Taking GPS IWV data as reference, the root-mean-square error (RMSE) has reduced 27.63% from 3.475 to 2.515 mm for Sentinel-3A, and 18.06% from 4.030 to 3.302 mm for Sentinel-3B. Taking ECMWF IWV data as reference, the RMSE was reduced by 25.27% from 3.490 to 2.608 mm for Sentinel-3A, and by 23.54% from 3.535 to 2.703 mm for Sentinel-3B. The improvement of OLCI IWV products was further confirmed in Mainland China, with smaller RMSE against reference IWV data from 214 GPS stations from June 1, 2019 to May 31, 2020.

***Keywords*:** GPS, integrated water vapor (IWV), Ocean and Land Color Instrument (OLCI).

***Editor in charge*: Dr. Dongkai Yang**

I. INTRODUCTION

Atmospheric water vapor plays a key role in observations of Earth's weather [1] and climate [2], [3], since it is the most abundant natural greenhouse gas [4], [5] and exerts significant effect on atmospheric moisture transportation and exchange of latent heat energy [6]. Usually, the distribution of atmospheric water vapor presents a large variability in both spatial and temporal domains [7], [8], which are closely associated with the changing weather and climate. In particular, its vertical profile is not evenly distributed in the atmospheric column [9]. The lower layers of atmosphere hold most of the water vapor, and the atmospheric water vapor concentration decreases sharply with height [9]. Consequently, accurate monitoring of atmospheric water vapor is fundamental and essential to obtain more understanding on the Earth's weather and climate system.

Water vapor is generally quantified using the integrated water vapor (IWV), also known as precipitable water vapor (PWV) and total column water vapor (TCWV) [10]. It is equivalent to condensing all the water vapor in the atmospheric column and measuring the height that it would reach in a vessel of unit cross section [11]. The unites are in columnar mass density (g/cm^2 or kg/m^2) or in length units (cm or mm).

The approaches to obtain IWV information are varied, including ground-based and satellite-based measurement techniques. Numerous ground-based observation approaches have been widely utilized for estimating IWV information, i.e., Global Navigation Satellite System (GNSS) [12]–[14], microwave radiometers [15], [16], radiosondes [17], [18], and sun photometers [19], [20]. Among the in-situ measurements of atmospheric water vapor, Global Positioning System (GPS) IWV observations have been checked as a reliable reference used for evaluating satellite-retrieved IWV observations [21]–

[23]. The spatial resolution of the GPS measurements depends significantly on the density of the in situ GPS networks available [22]. In addition, the most common observation approach to observe atmospheric water vapor is through remote sensing, as it can provide continuous IWV observations on a global basis [24]. Satellite-based remote sensing techniques are divided into four types according to the different retrieval bands: the visible (VIS) retrieval method [25], [26], the near-infrared (NIR) retrieval method [27], [28], the infrared (IR) retrieval method [29], [30], and the microwave (MW) retrieval method [31], [32]. When the VIS or NIR channels are used, the retrieval accuracy of satellite-based remote sensing IWV observations is usually poor under cloudy conditions due to the effect of the opacity of clouds [25]–[28].

European Space Agency (ESA) has developed the Sentinel-3 family to support the climate monitoring [33]. The Sentinel-3 satellites were launched on February 16, 2016 (Sentinel-3A) and April 25, 2018 (Sentinel-3B), respectively. The Ocean and Land Color Instrument (OLCI) on board Sentinel-3A and Sentinel-3B is based on the heritage of the Medium Resolution Imaging Spectrometer (MERIS) on board the Envisat satellite [34]. Its main difference with its predecessor is that OLCI sensor has 21 spectral channels, in contrast to the 15 spectral channels on MERIS sensor [34]. An operational water vapor retrieval approach has been proposed for OLCI instrument to retrieve IWV data over land, ocean, and clouds at a global coverage [35]. Two NIR channels located at 900 nm (water vapor absorption channel) and 885 nm (window channel) were used [35]. This retrieval method relies upon the differential absorption approach [36] to relate the IWV estimation to the measured radiance ratio of OLCI NIR channels O19 (900 nm) and O18 (885 nm) [35]. The retrieved OLCI IWV products published by the Sentinel-3 satellites were usually generated with a spatial resolution of 300 m [37] using a neural network and a Matrix Operator Model (MOMO) [35]. Compared with other satellite-based remote sensing IWV observations with a spatial resolution of 1000 m, e.g., Moderate Resolution Imaging Spectroradiometer (MODIS) on-board Aqua and Terra satellites [38]–[40] and Medium Resolution Imaging Spectrometer (MERSI) on-board Fengyun-3 (FY-3) satellites [41]–[43], the higher spatial-resolution OLCI water vapor data can provide more detailed water vapor distribution information for the climate studies, especially regional climate change monitoring.

It is known that the high-accuracy water vapor observations from space-based instruments are more beneficial to study the weather and climate at both global and local scales, since satellite-based remote sensing IWV observations can provide continuous water vapor distribution information at an adequate spatial and temporal resolution [22]. Previous findings showed that, under clear land conditions, the bias for OLCI IWV products was -0.57±2.90 mm for Sentinel-3A and +2.42±3.41 mm for Sentinel-3B in Crete, Greece, by comparing against in-situ GNSS-derived IWV data [44]. Although the accuracy of the operational OLCI IWV products has been proved good in clear land conditions, the retrieval accuracy of the OLCI IWV products under non-clear land conditions (e.g., under cloudy conditions) is usually poor because the NIR channels of the OLCI instrument used for water vapor retrieval [35] cannot penetrate the clouds. It is necessary to further improve the accuracy of current OLCI IWV products to serve better for the observations of weather and climate. However, there has been no publication related to the improvement of Sentinel-3 OLCI IWV products, especially under non-clear land conditions.

In this study, we developed a model to retrieve the improved Sentinel-3 OLCI IWV observations under clear and non-clear land conditions. The approach was based on the regression fitting between the differential water vapor information against the official OLCI IWV products. The differential IWV data were calculated from the operational OLCI IWV products and a reliable reference such as in-situ GPS-derived high-accuracy IWV data. The OLCI IWV pixels were divided into two groups according to the quality flag of each pixel. For each group, the empirical regression relationship between the differential IWV data against the official Sentinel-3 OLCI IWV products was defined, and the regression model coefficients were calculated for each season.

Section II provided a detailed description of the data sets used in model development and evaluation. The methodologies for water vapor retrieval from ground-based GPS measurements, and the improvement of the operational Sentinel-3 OLCI IWV products were presented in Section III. It also presented the statistical metrics used for evaluating the accuracy of the calibrated OLCI IWV data. In Section IV, the validation results between the calibrated Sentinel-3 OLCI IWV data against GPS-derived IWV observations and European Centre for Medium-Range Weather Forecasts (ECMWF) reanalysis IWV data were analyzed and discussed. Section V summarized the key conclusions in this study.

II. Data and Pre-Processing

The study area in this research has two parts, i.e., Australia and Mainland China. The study area in Australia ranges from 10°41’ S to 43°39’ S, and from 112°57’ E to 153°45’ E. The study area in Mainland China covers the interior and coastal areas with latitude ranging from 16°42’ N to 53°33’ N, and longitude ranging from 73°40’ E to 135°03’ E. A total of 667 ground-based GPS sites were employed in this study, with 453 of these stations located in Australia, and 214 stations located in Mainland China. The detailed description of the research area and the geographic locations of in-situ GPS sites are displayed in Fig. 1. The ground-based GPS sites in Australia were utilized to develop the model for calibrating the official OLCI IWV products, as well as to evaluate the accuracy of the calibrated water vapor data retrieved from the operational OLCI IWV products. The in-situ GPS stations situated in Mainland China were used to evaluate the performance of the developed model in different regions. In this paper, we used three types of data collected during the period between June 1, 2018 and May 31, 2020, including ground-based GPS measurements, Level-2 IWV products from Sentinel-3 OLCI observations, and IWV data from ECMWF reanalysis products. A summary of the characteristics of the data sets used in this research is shown in Table I.

A. GPS IWV Data

The in-situ water vapor data, retrieved from the Geoscience Australia [45] and the Crustal Movement Observation Network of China (CMONOC) [46] GPS measurements, were utilized to construct and validate the model of calibrating current Level-2 OLCI IWV products. In this work, the ground-based IWV data were calculated from zenith total delay (ZTD) products provided by Geoscience Australia and CMONOC, with a temporal resolution of 1 h. The detailed information of this calculation process is described in Section III. As presented in Table I, the ground-based GPS-retrieved IWV observations from June 1, 2018 to May 31, 2019 from 453 GPS sites over Australia were employed for model development. The in-situ GPS-derived IWV data for the whole year (from June 1, 2019 to May 31, 2020) from 667 GPS sites over Australia and Mainland China were employed for model evaluation.

In the model development and validation, the time difference between the observations of GPS IWV and OLCI IWV is required to be smaller than 30 minutes in this work.

B. OLCI IWV Data

The OLCI sensor onboard Sentinel-3A and Sentinel-3B evolves from the MERIS sensor onboard the Envisat satellite. Retrieval of atmospheric water vapor content from Sentinel-3 OLCI observations mainly uses two NIR channels, i.e., an absorption channel located at 900 nm and a window channel located at 885 nm. The calculation of this retrieval method is based on a neural network and a matrix operator model (MOMO) [35]. The IWV data from the Sentinel-3 OLCI Level-2 Land Full Resolution (OL_2_LFR) products with a spatial resolution of 300 m [37] were employed in this study,. All Level-2 Sentinel-3A and Sentinel-3B OLCI IWV products used in this research, were collected from the ESA Copernicus Open Access Hub (https://scihub.copernicus.eu/dhus/#/home). As shown in Table I, the OLCI IWV data between June 1, 2018 and May 31, 2019 over Australia were used for model development and the OLCI IWV data between June 1, 2019 to May 31, 2020 over Australia and Mainland China were used for model validation. In addition, the Level-2 OLCI product file “LQSF” was employed as a classification flag mask to obtain the quality of each IWV pixel.

C. ECMWF IWV Data

The fifth generation of ECMWF Reanalysis (ERA5) [47], [48] water vapor data were also utilized to assess the performance of the developed model in this research, which were obtained from the Climate Data Store (CDS) (https://cds.climate.copernicus.eu/#!/home). The ERA5 IWV data were generated with a temporal resolution of 1 h and a spatial resolution of 0.25° x 0.25° using the 4D-Var assimilation approach. As displayed in Table I, the ERA5 reanalysis IWV data during the period between June 1, 2019 and May 31, 2020 over Australia were collected as the second dataset for model evaluation. This comparison analysis is based on the locations of the in-situ 453 GPS sites in Australia.

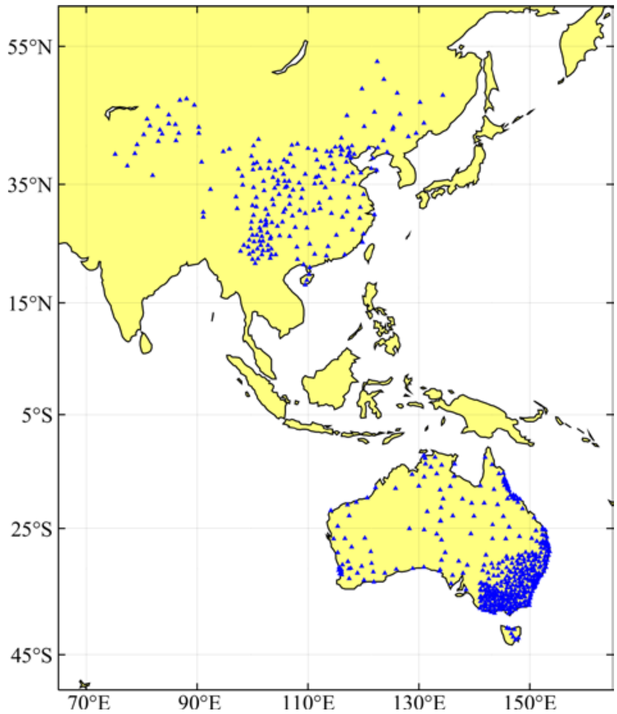

Fig. 1. Distribution map of the in-situ GPS stations in inland and coastal areas of Australia and Mainland China. 453 of these sites are situated in Australia, with 214 sites situated in Mainland China.

TABLE I

TABLE I SUMMARY OF DATA CHARACTERISTICS USED FOR MODEL DEVELOPMENT AND VALIDATION COLLECTED DURING THE PERIOD FROM JUNE 1, 2018 TO MAY 31, 2020 IN AUSTRALIA AND MAINLAND CHINA

Data source	Time span	Temporal resolution	Spatial resolution	Data description	Function	Region
GPS data	June 1, 2018~May 31, 2019	hourly	453 sites, point data	meteorology data	model construction	Australia
OLCI Level-2 product		4-day	300 m	IWV data		Australia
GPS data	June 1, 2019~May 31, 2020	hourly	667 sites, point data	meteorology data	model evaluation	Australia; Mainland China
OLCI Level-2 product		4-day	300 m	IWV data		Australia; Mainland China
ECMWF IWV product		hourly	0.25° x 0.25°	IWV columns		Australia

III. METHODS

A. *Ground-based IWV Retrieval from GPS Observations*

Retrieval of IWV data from GPS measurements mainly relies upon the propagation delays, which is caused by the neutral atmosphere. This slant tropospheric delay (STD) can be converted to the zenith tropospheric delay (ZTD) using the mapping function [49], [50], which can be separated into zenith hydrostatic delay (ZHD) and zenith wet delay (ZWD). The tropospheric gases are responsible for the ZHD, and its calculation equation is defined as follows [49]:

$$ZHD = (2.2997 \pm 0.0024)P_s / f(\theta, H) \tag{1}$$

$$f(\theta, H) = 1 - 0.00266 \cos 2\theta - 0.00028H \tag{2}$$

where P_s is the atmospheric pressure, θ is the latitude, and H is the height. The atmospheric water vapor is mainly responsible for the ZWD. The retrieved IWV data from GPS observations can be determined as follows [49]:

$$IWV = \Pi \cdot ZWD \tag{3}$$

where the Π is a scale parameter calculated from surface temperature [51].

In the ground-based GPS IWV calculation, the surface temperature and atmospheric pressure from ECMWF reanalysis products were employed to calculate the ZHD and the parameter Π. When the ZHD and Π were calculated, ground-based GPS IWV data were derived from Geoscience Australia and CMONOC ZTD products. The in-situ water vapor data from 667 GPS sites over Australia and Mainland China were selected for developing and evaluating the model in this research.

B. *Methodology for the Improvement of OLCI IWV Products*

To improve the accuracy of the official IWV products derived from OLCI instrument, we developed a calibrated model for calculating the improved water vapor data from the operational OLCI IWV products. The flowchart of the model is illustrated in Fig. 2, and the key steps for the model development are described as follows.

According to the performance of the OLCI IWV products under different weather conditions, the OLCI IWV pixels were classified into two categories according to the quality flag file "LQSF". The OLCI IWV pixels flagged as "LAND" were considered as the "Land" group. The "LAND" pixels implied that the OLCI IWV products were retrieved in the clear land conditions. The OLCI IWV pixels flagged as others such as "CLOUD", "SNOW_ICE", and "WATER", were considered as the "Non-land" group. This implied that the OLCI IWV products were retrieved under non-clear land conditions. For these two groups, the OLCI IWV pixels closest to each in-situ GPS site were selected for model development.

Then, we calculated the differential water vapor information using the spatially and temporally collocated OLCI-derived IWV products and GPS-observed IWV data. The GPS IWV observations were considered as the in-situ truth in this calculation. For each group, the differential IWV for each OLCI IWV pixel were defined as:

$$\Delta IWV = IWV_{OLCI} - IWV_{GPS} \tag{4}$$

where ΔIWV is the differential IWV, IWV_{OLCI} is the IWV from the official OLCI IWV products, and IWV_{GPS} is the IWV from the reference GPS-retrieved IWV data.

For each group, we studied the relationship between the differential IWV (ΔIWV) and the official OLCI IWV products from Sentinel-3A and Sentinel-3B. The regression analysis utilized the spatio-temporally collocated OLCI-GPS IWV data from June 1, 2018 to May 31, 2019 in Australia, i.e., training datasets. As shown in Fig. 3, for both Sentinel-3A and Sentinel-3B satellites, the empirical relationships between the differential IWV and the operational OLCI IWV products were individually analyzed for Land and Non-land group. Evidently, they can be very well defined using a linear function. Hence, the empirical equation between the differential IWV data and the official Sentinel-3 OLCI IWV products for both Land and Non-land groups can be written as:

$$\Delta IWV = a \cdot IWV_{OLCI} + b \tag{5}$$

where a and b are the empirical regression parameters. When the differential IWV information is obtained, the calibrated IWV can be calculated from the official Sentinel-3 OLCI IWV products using the equation as follows:

$$IWV_c = IWV_{OLCI} - \Delta IWV \tag{6}$$

where IWV_c is the calibrated IWV estimated from OLCI IWV products. The essential step of the developed model is to obtain the regression coefficients from the GPS-retrieved IWV data and the operational OLCI IWV products. Once the parameters a and b are calculated, we can calibrate the OLCI IWV products and obtain the calibrated OLCI IWV data.

However, due to the annual cycle of the atmospheric water vapor, satellite-sensed IWV observations usually display a dependence on the different seasons [22], [23]. To obtain more accurate regression parameters a and b, we calculated them from each season from the training datasets (i.e., the official Sentinel-3 OLCI IWV products and the reference GPS-derived IWV data from June 1, 2018 to May 31, 2019 in Australia) in this study. The seasons in Australia are defined as spring (September to November), summer (January, February, and December), autumn (March to May), and winter (June to August). When the seasonal parameters a and b were calculated, we used them to calibrate the official OLCI IWV products published by Sentinel-3.

C. *Statistical Analysis*

In this paper, we used three statistical parameters to evaluate the accuracy of the official Sentinel-3 OLCI IWV products and the calibrated OLCI IWV data, by conducting comparisons with the reliable references such as GPS-retrieved IWV data and reanalysis ERA5 IWV products. The OLCI IWV pixels closest to the ground-based GPS stations were selected for model validation. The statistical metrics include the coefficient of determination (R^2), root-mean-square error (RMSE), and mean bias (MB). The metrics are defined as:

$$R^2 = \left[\frac{\sum_{i=1}^{N}(IWV_R - \overline{IWV_R})(IWV_O - \overline{IWV_O})}{\sqrt{\sum_{i=1}^{N}(IWV_R - \overline{IWV_R})^2(IWV_O - \overline{IWV_O})^2}}\right]^2 \tag{7}$$

$$RMSE = \sqrt{\frac{1}{N}\sum_{i=1}^{N}(IWV_R - IWV_O)^2} \tag{8}$$

$$MB = \frac{1}{N}\sum_{i=1}^{N}(IWV_O - IWV_R) \tag{9}$$

where N is the number of data pairs, IWV_R is the reference IWV obtained from GPS or ERA5, $\overline{IWV_R}$ is the mean IWV averaged from reference GPS or ERA5, IWV_O is the observed IWV obtained from OLCI, and $\overline{IWV_O}$ is the mean IWV averaged from OLCI. R^2 indicates the strength of the linear relationship between the OLCI IWV data and reference GPS or ERA5 IWV data. RMSE shows the overall difference between the paired IWV data sets. MB provides the information on the overestimation or underestimation of the OLCI IWV data against reference GPS or ERA5 IWV data. In an ideal state, i.e., $R^2 = 1$, RMSE = 0, MB = 0, and the slopes and intercepts of the linear regression lines are 1 and 0, it illustrates that the OLCI-observed water vapor values are exactly equal to the reference truth values, e.g., GPS and ERA5 water vapor data.

Fig. 2. Flowchart of the model developed in this research to obtain the improved water vapor data from the official Sentinel-3 OLCI IWV products.

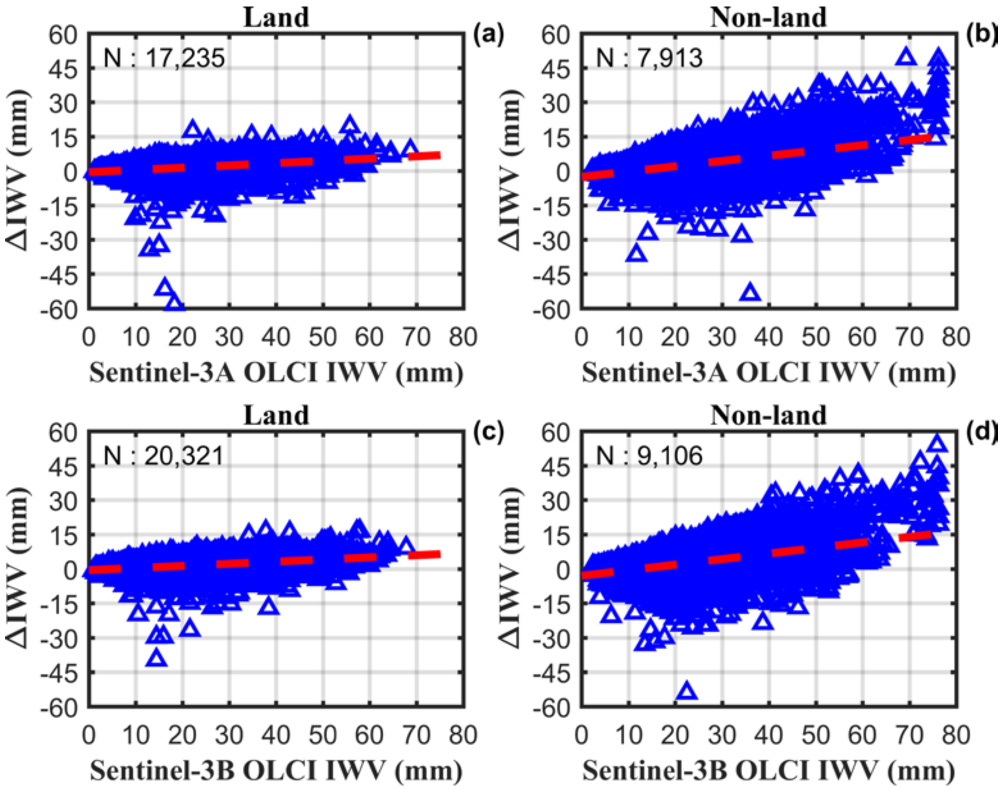

Fig. 3. Regression analysis between the differential water vapor data estimated from the official Sentinel-3 OLCI IWV products and the reference GPS IWV data against the official Sentinel-3 OLCI IWV products. (a) and (b): Scatter points of the differential IWV versus the official Sentinel-3A OLCI IWV products for Land and Non-land groups. (c) and (d): Scatter points of the differential IWV versus the official Sentinel-3B OLCI IWV products for Land and Non-land groups. N is the number of collocated data points used for regression analysis. The dashed red lines represent the empirical regression fitting.

IV. RESULTS

In order to assess the performance of the developed model on calibrating the Sentinel-3 OLCI IWV products, the calibrated OLCI IWV data over Australia were compared with two reliable references, i.e., GPS-retrieved IWV data and ERA5 IWV data. In addition, evaluation of the calibrated IWV data and in-situ GPS IWV data was further implemented in Mainland China. The calibrated IWV data in the model validation was retrieved using the seasonal regression parameters, calculated from the training datasets between June 1, 2018 and May 31, 2019 over Australia. A total of 667 GPS sites (i.e., 453 stations in Australia and 214 stations in Mainland China) was utilized for the model validation in this work.

A. *Comparison of GPS IWV Data versus OLCI IWV Products in Australia*

The water vapor data from OLCI and GPS from June 1, 2018 to May 31, 2019 from 453 GPS sites over Australia were employed as the training datasets for the model construction in this research. After regression analysis, we have obtained the regression equation as well as regression coefficients for both Land and Non-land groups. We recalculated the OLCI IWV data from the training datasets using the seasonal regression coefficients, with results shown in Figs. 4 and 5. The recalculation results from June 1, 2018 to May 31, 2019 over Australia indicated that the calibrated OLCI IWV data perform better than the operational OLCI IWV products for both Land and Non-land groups, with higher correlations and lower RMSE against the reference GPS-derived IWV data. For Land group, the slop and intercept of the regression lines for the in-situ GPS-retrieved IWV versus operational OLCI IWV products were 0.901 and 0.554 for Sentinel-3A, and 0.907 and 0.544 for Sentinel-3B, respectively. The slopes and intercepts of the linear regression lines for the calibrated IWV data were both equal to 1 (1.000 and 1.000) and around 0 (0.001 and 0.002). The R^2 values for the operational OLCI IWV products and the calibrated IWV data were 0.952 and 0.954 for Sentinel-3A, and 0.942 and 0.944 for Sentinel-3B. The RMSE values were reduced by 23.28% from 2.496 to 1.915 mm for Sentinel-3A, and 18.37% from 2.679 to 2.187 mm for Sentinel-3B. The MB values were reduced greatly after the model calibration. For Non-land group, the slope of the calibrated Sentinel-3 OLCI IWV data was also close to 1. The RMSE for Sentinel-3A were reduced by 22.69% from 6.020 to 4.654 mm, with the reduction of 22.42% from 6.151 to 4.772 mm for Sentinel-3B. The MB values were also reduced. For all OLCI IWV pixels obtained from both Land and Non-land groups, the RMSE were reduced by 22.86% from 3.959 to 3.054 mm for Sentinel-3A, and 21.19% from 4.082 to 3.217 mm for Sentinel-3B.

In addition, we applied the seasonal regression parameters to the operational OLCI IWV products from June 1, 2019 to May 31, 2020 over Australia. The calibrated OLCI IWV data were evaluated by ground-based water vapor data derived from 453 GPS stations. The evaluation results between June 1, 2019 and May 31, 2020 over Australia were displayed in Figs. 6 and 7. For Land group, the RMSE has reduced 28.56% from 2.188 to 1.563 mm for Sentinel-3A, and 10.79% from 3.354 to 2.992 mm for Sentinel-3B. For Non-land group, the RMSE has reduced 27.28% from 5.311 to 3.862 mm for Sentinel-3A, and 25.50% from 5.267 to 3.924 mm. For all OLCI IWV pixels, the RMSE has reduced 27.63% from 3.475 to 2.515 mm for Sentinel-3A, and 18.06% from 4.030 to 3.302 mm for Sentinel-3B. The slopes and intercepts of the linear regression lines for the calibrated OLCI IWV data were in the range of 0.974 to 1.015, and -0.439 to 0.085, respectively. The MB values for the calibrated OLCI IWV data and the official OLCI IWV products were all positive, implying that the Sentinel-3 OLCI IWV retrievals tended to overestimate IWV values. The evaluation results from June 1, 2019 to May 31, 2020 over Australia indicated that the calibrated OLCI IWV data in this study has superior accuracy than the official OLCI IWV products, when compared with ground-based GPS-retrieved IWV data.

Furthermore, the seasonal comparison analysis between the OLCI IWV data and the reference GPS-derived IWV data is also conducted, with seasonal evaluation results presented in Table II. For the period from June 1, 2018 to May 31, 2019 in Australia, the official Sentinel-3 OLCI IWV products were significantly improved in each season, and the RMSE was reduced by 16.11% from 3.675 to 3.083 mm in spring, by 21.32% from 4.302 to 3.385 mm in summer, by 28.25% from 4.326 to 3.104 mm in autumn, and by 33.33% from 2.958 to 1.972 mm in winter for Sentinel-3A, and it was reduced by 18.25% from 3.479 to 2.844 mm, by 19.94% from 4.338 to 3.473 mm, by 22.19% from 4.785 to 3.723 mm, and by 33.50% from 3.060 to 2.035 mm for Sentinel-3B, respectively. The seasonal slopes and intercepts of the calibrated OLCI IWV data were all equal to 1.000 and around 0 for both Sentinel-3A and Sentinel-3B satellites. For the period from June 1, 2019 to May 31, 2019 over Australia, the seasonal maximum RMSE reduction was 36.18% from 2.908 to 1.856 mm in winter for Sentinel-3A satellite, and 27.26% from 4.131 to 3.005 mm in autumn for Sentinel-3B satellite. The seasonal minimum RMSE reduction was in spring for both Sentinel-3A and Sentinel-3B satellites, with an RMSE reduction of 16.92% from 2.684 to 2.230 mm for Sentinel-3A and 6.34% from 4.576 to 4.286 mm for Sentinel-3B.

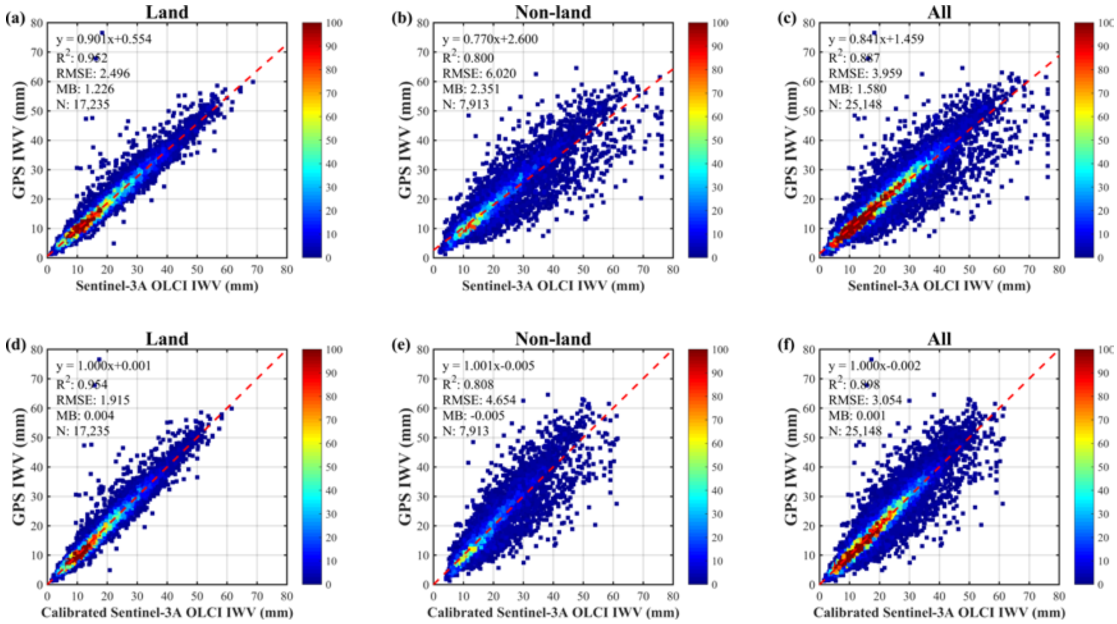

Fig. 4. Comparison of the ground-based GPS-derived IWV data against the official Sentinel-3A OLCI IWV products (first row) and the calibrated Sentinel-3A OLCI IWV data (second row) from June 1, 2018 to May 31, 2019 in Australia. (a) and (d): Scatter plots between GPS IWV against the official Sentinel-3A OLCI IWV and the calibrated Sentinel-3A OLCI IWV for Land group. (b) and (e): Scatter plots between GPS IWV against the official Sentinel-3A OLCI IWV and the calibrated Sentinel-3A OLCI IWV for Non-land group. (c) and (f): Scatter plots between GPS IWV against the official Sentinel-3A OLCI IWV and the calibrated Sentinel-3A OLCI IWV for all OLCI IWV pixels. All OLCI IWV pixels are obtained from both Land and Non-land groups. N is the number of collocated GPS-OLCI data points used for comparison analysis. The dashed red lines represent the linear regression of these data. The points coloured with a rainbow scale illustrate the frequency of the OLCI IWV values (brown most frequent, blue least frequent).

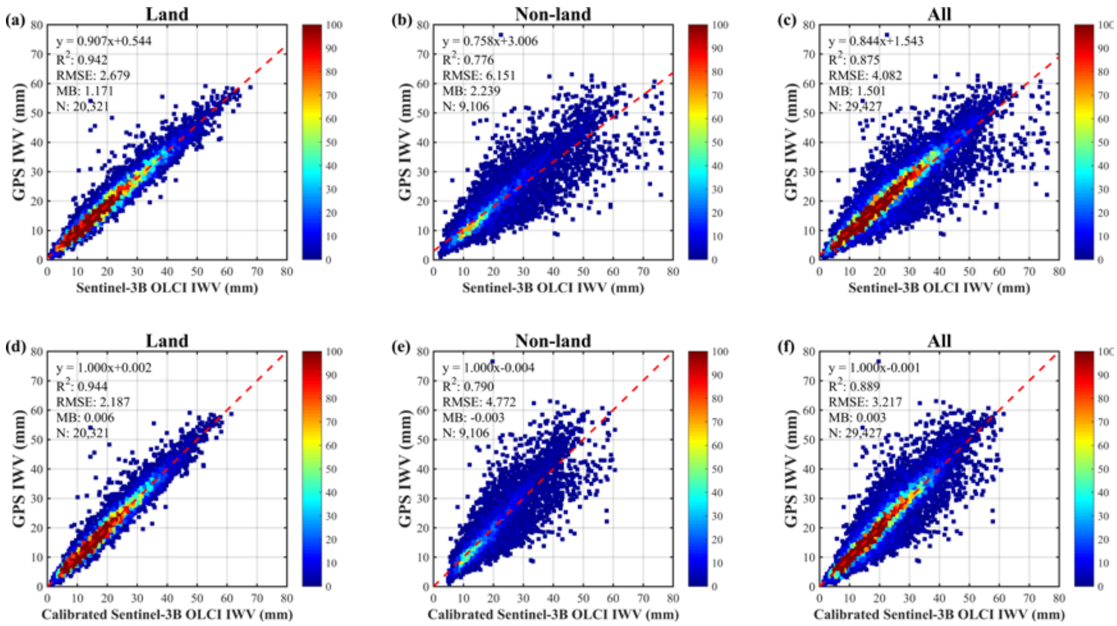

Fig. 5. Comparison of the ground-based GPS-derived IWV data against the official Sentinel-3B OLCI IWV products (first row) and the calibrated Sentinel-3B OLCI IWV data (second row) from June 1, 2018 to May 31, 2019 in Australia. (a) and (d): Scatter plots between GPS IWV against the official Sentinel-3B OLCI IWV and the calibrated Sentinel-3B OLCI IWV for Land group. (b) and (e): Scatter plots between GPS IWV against the official Sentinel-3B OLCI IWV and the calibrated Sentinel-3B OLCI IWV for Non-land group. (c) and (f): Scatter plots between GPS IWV against the official Sentinel-3B OLCI IWV and the calibrated Sentinel-3B OLCI IWV for all OLCI IWV pixels. All OLCI IWV pixels are obtained from both Land and Non-land groups. N is the number of collocated GPS-OLCI data points used for comparison analysis. The dashed red lines represent the linear regression of these data. The points coloured with a rainbow scale illustrate the frequency of the OLCI IWV values (brown most frequent, blue least frequent).

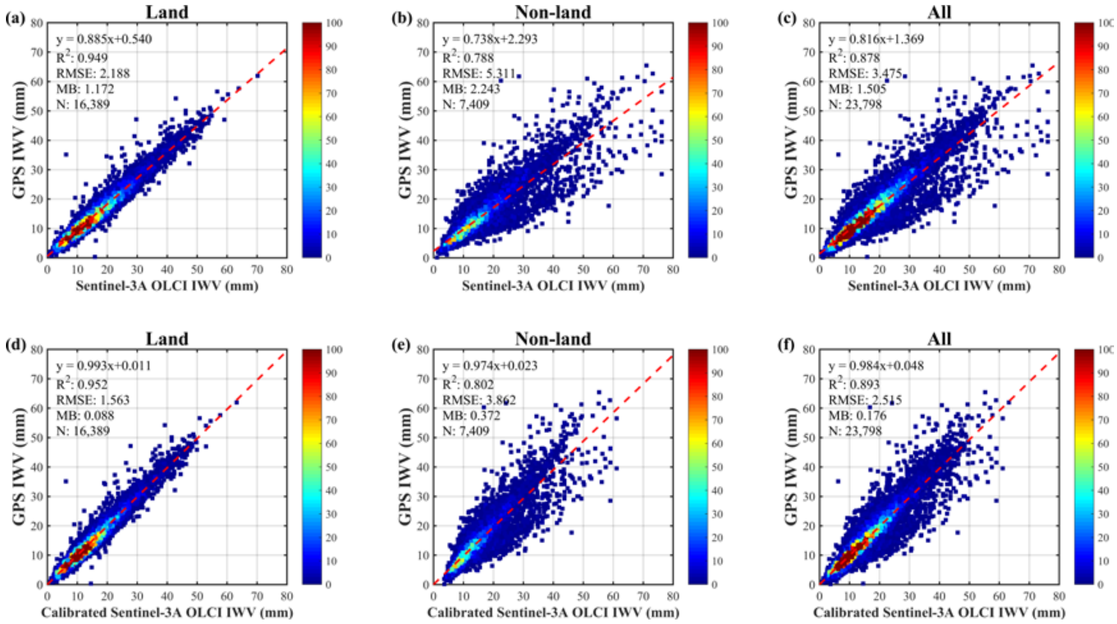

Fig. 6. Comparison of the ground-based GPS-derived IWV data against the official Sentinel-3A OLCI IWV products (first row) and the calibrated Sentinel-3A OLCI IWV data (second row) from June 1, 2019 to May 31, 2020 in Australia. (a) and (d): Scatter plots between GPS IWV against the official Sentinel-3A OLCI IWV and the calibrated Sentinel-3A OLCI IWV for Land group. (b) and (e): Scatter plots between GPS IWV against the official Sentinel-3A OLCI IWV and the calibrated Sentinel-3A OLCI IWV for Non-land group. (c) and (f): Scatter plots between GPS IWV against the official Sentinel-3A OLCI IWV and the calibrated Sentinel-3A OLCI IWV for all IWV pixels. All OLCI IWV pixels are obtained from both Land and Non-land groups. N is the number of collocated GPS-OLCI data points used for comparison analysis. The dashed red lines represent the linear regression of these data. The points coloured with a rainbow scale illustrate the frequency of the OLCI IWV values (brown most frequent, blue least frequent).

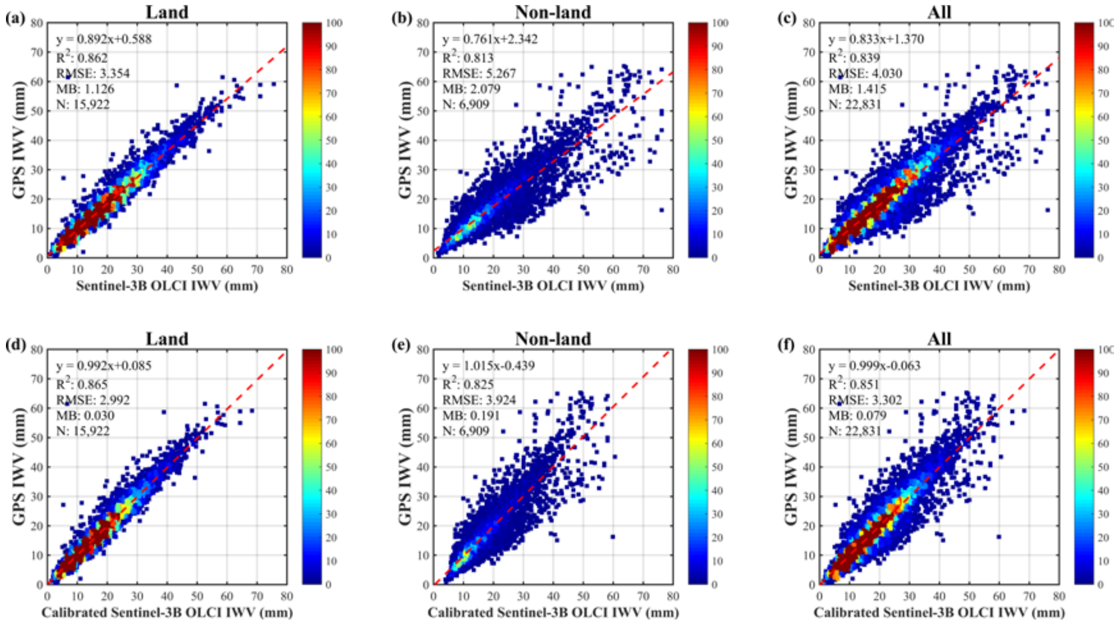

Fig. 7. Comparison of the ground-based GPS-derived IWV data against the official Sentinel-3B OLCI IWV products (first row) and the calibrated Sentinel-3B OLCI IWV data (second row) from June 1, 2019 to May 31, 2020 in Australia. (a) and (d): Scatter plots between GPS IWV against the official Sentinel-3B OLCI IWV and the calibrated Sentinel-3B OLCI IWV for Land group. (b) and (e): Scatter plots between GPS IWV against the official Sentinel-3B OLCI IWV and the calibrated Sentinel-3B OLCI IWV for Non-land group. (c) and (f): Scatter plots between GPS IWV against the official Sentinel-3B OLCI IWV and the calibrated Sentinel-3B OLCI IWV for all IWV pixels. All OLCI IWV pixels are obtained from both Land and Non-land groups. N is the number of collocated GPS-OLCI data points used for comparison analysis. The dashed red lines represent the linear regression of these data. The points coloured with a rainbow scale illustrate the frequency of the OLCI IWV values (brown most frequent, blue least frequent).

TABLE II THE SEASONAL EVALUATION AGAINST REFERENCE GPS-RETRIEVED IWV DATA DURING THE PERIOD BETWEEN JUNE 1, 2018 TO MAY 31, 2020 OVER AUSTRALIA. ALL OLCI IWV PIXELS OBTAINED FROM BOTH LAND AND NON-LAND GROUPS WERE USED

Time span		OLCI product	Sentinel-3A					Sentinel-3B				
			Slope	Intercept	R^2	RMSE	MB	Slope	Intercept	R^2	RMSE	MB
June 1, 2018 to May 31, 2019	Spring	OLCI L2 IWV	0.848	1.352	0.867	3.675	1.165	0.835	1.561	0.864	3.479	1.120
		Calibrated OLCI IWV	1.000	-0.001	0.874	3.083	0.003	1.000	-0.002	0.874	2.844	0.005
	Summer	OLCI L2 IWV	0.820	2.781	0.867	4.302	1.652	0.821	3.064	0.86	4.338	1.523
		Calibrated OLCI IWV	1.000	-0.004	0.873	3.385	0.000	1.000	-0.002	0.868	3.473	0.006
	Autumn	OLCI L2 IWV	0.818	1.645	0.884	4.326	2.097	0.813	1.669	0.835	4.785	2.045
		Calibrated OLCI IWV	1.000	-0.002	0.893	3.104	0.001	1.000	-0.001	0.845	3.723	-0.003
	Winter	OLCI L2 IWV	0.74	1.835	0.811	2.958	1.344	0.728	2.106	0.796	3.060	1.238
		Calibrated OLCI IWV	1.000	0.000	0.838	1.972	-0.002	1.000	0.000	0.833	2.035	0.002
June 1, 2019 to May 31, 2020	Spring	OLCI L2 IWV	0.843	1.444	0.878	2.684	0.685	0.826	1.799	0.681	4.576	0.593
		Calibrated OLCI IWV	0.984	0.258	0.888	2.230	-0.049	0.981	0.364	0.689	4.286	-0.123
	Summer	OLCI L2 IWV	0.850	1.758	0.911	3.941	1.41	0.832	2.431	0.896	3.618	1.343
		Calibrated OLCI IWV	1.039	-1.104	0.911	3.240	0.315	1.021	-0.778	0.900	2.863	0.330
	Autumn	OLCI L2 IWV	0.791	1.783	0.847	4.317	2.259	0.819	1.461	0.871	4.131	2.057
		Calibrated OLCI IWV	0.976	0.028	0.860	3.019	0.388	1.008	-0.243	0.880	3.005	0.107
	Winter	OLCI L2 IWV	0.761	1.420	0.837	2.908	1.476	0.777	1.452	0.735	3.591	1.327
		Calibrated OLCI IWV	1.009	-0.227	0.866	1.856	0.128	1.012	-0.214	0.754	2.903	0.081

B. Comparison of ERA5 IWV Data versus OLCI IWV Products in Australia

In order to further evaluate the performance of the model, validation against additional reanalysis ECMWF IWV data over Australia is conducted in this research. This comparison analysis was performed at the locations of ground-based 453 GPS sites in Australia.

As shown in Figs. 8 and 9, the recalculation results from June 1, 2018 to May 31, 2019 were compared against ERA5 IWV data over Australia. In Fig. 8, the comparison results between the calibrated Sentinel-3A OLCI IWV data against ERA5 IWV products showed a higher accuracy compared with the official Sentinel-3A OLCI IWV products in terms of the RMSE. The RMSE has reduced 21.05% from 2.594 to 2.048 mm for Land group, 24.12% from 5.858 to 4.446 mm for Non-land group, and 23.18% from 3.926 to 3.016 mm for all OLCI IWV pixels calculated from both Land and Non-land groups. After the model calibration, the Sentinel-3A OLCI IWV products had better agreements with ERA5 IWV data with the slopes close to 1 (from 0.964 to 0.979). The MB values were calibrated from positive (overestimated) to negative (underestimated). Similarly, for Sentinel-3B (see Fig. 9), the RMSE has reduced 19.19% from 2.678 to 2.164 mm for Land group, 22.58% from 6.125 to 4.742 mm for Non-land group, and 21.53% from 4.069 to 3.193 mm for all OLCI IWV pixels, respectively. The slopes of the linear regression lines for the calibrated IWV data were both closer to 1, with the MB values varying from positive values (overestimated) to negative values (underestimated). The calibrated Sentinel-3 OLCI IWV results from June 1, 2018 to May 31, 2019 indicated that the calibrated OLCI IWV data agrees quiet well with the reanalysis ERA5 IWV data, with the large reduction of the RMSE values.

The calibrated Sentinel-3 OLCI IWV data between June 1, 2019 and May 31, 2020 over Australia calculated from the seasonal regression coefficients were compared against ECMWF reanalysis IWV data, with results shown in Figs. 10 and 11. The validation results indicated that the calibrated Sentinel-3 OLCI IWV data improved the accuracy of the official Sentinel-3 OLCI IWV products, and reduced the RMSE by 23.08% from 2.283 to 1.756 mm for Land group, 26.21% from 5.253 to 3.876 mm for Non-land group, and 25.27% from 3.490 to 2.608 mm for all IWV pixels for Sentinel-3A, and 19.73% from 2.377 to 1.908 mm, 25.35% from 5.318 to 3.970 mm, and 23.54% from 3.535 to 2.703 mm for Sentinel-3B, respectively. The slopes and intercepts of the linear regression lines for the calibrated Sentinel-3A OLCI IWV data were 0.956 and 0.822 for Land group, 0.949 and 0.859 for Non-land group, and 0.953 and 0.843 for all IWV pixels, respectively; similarly, the slopes and intercepts of the linear regression lines for the calibrated Sentinel-3B OLCI IWV data were 0.965 and 0.775, 0.985 and 0.411, and 0.972 and 0.664, respectively. The calibrated Sentinel-3 OLCI IWV products had negative MB values (underestimated), with the operational Sentinel-3 OLCI IWV products having positive MB values (overestimated). Hence, the calibrated Sentinel-3 OLCI IWV data in this study has superior accuracy than the official Sentinel-3 OLCI IWV products, when compared with reference ERA5 IWV data.

Moreover, the recalculated results, i.e., from June 1, 2018 to May 31, 2019 over Australia, and the evaluation results, i.e., from June 1, 2019 to May 31, 2020 over Australia, were also compared against the reference ERA5 IWV data at a seasonal basis. The seasonal comparison analysis results shown in Table III implied that, for each season, the calibrated Sentinel-3 OLCI IWV products against the reference ERA5 IWV data have a higher accuracy than those of the official Sentinel-3 OLCI IWV products in terms of the RMSE values. For the seasonal recalculation results between June 1, 2018 and May 31, 2019 over Australia, the seasonal maximum RMSE reduction occurred in winter for both Sentinl-3A and Sentinel-3B, and reduced the RMSE by 31.23% from 2.815 to 1.936 mm for Sentinel-3A satellite and by 31.42% from 2.947 to 2.021 mm for Sentinel-3B satellite. The seasonal minimum RMSE reduction occurred in spring for Sentinel-3 satellites, with an RMSE reduction of 18.32% (from 3.509 to 2.866 mm) for Sentinel-3A and 20.08% (from 3.486 to 2.786 mm) for Sentinel-3B. For the seasonal evaluation results between June 1, 2019 and May 31, 2020 over Australia, the seasonal maximum RMSE reduction was 33.69% from 2.710 to 1.797 mm for Sentinel-3A and 28.61% from 2.810 to 2.006 mm for Sentinel-3B, both in winter. The seasonal minimum RMSE reduction was 15.16% from 2.744 to 2.328 mm for Sentinel-3A and 19.37% from 2.902 to 2.340 mm for Sentinel-3B, both in spring. For Sentinel-3 satellites, the seasonal slopes were calibrated to be closer to 1.

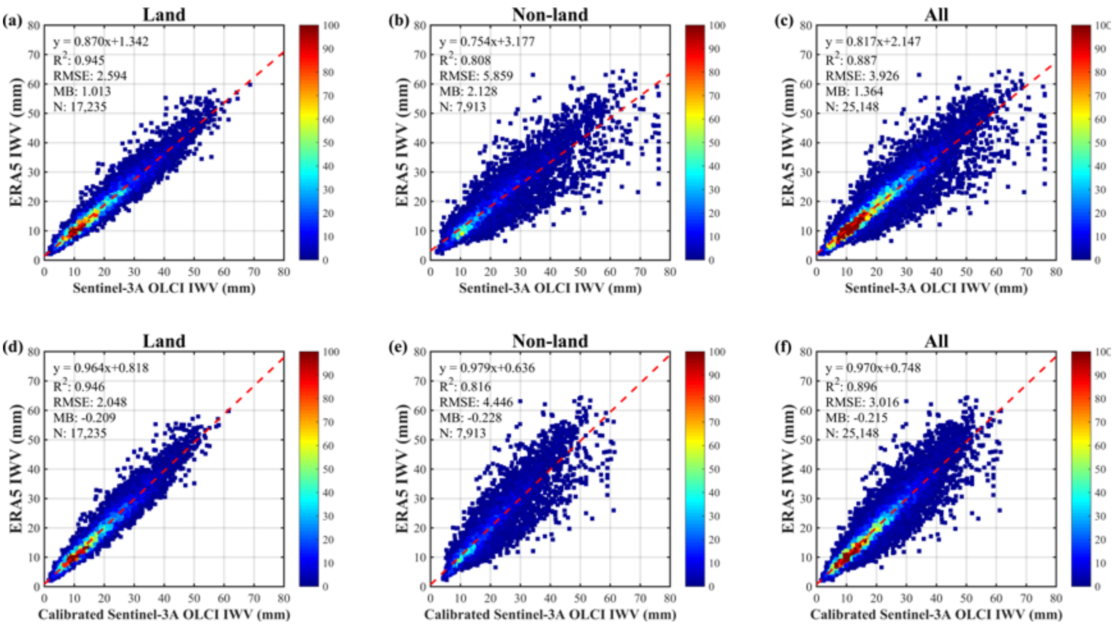

Fig. 8. Comparison of the ERA5 IWV data against the official Sentinel-3A OLCI IWV products (first row) and the calibrated Sentinel-3A OLCI IWV data (second row) from June 1, 2018 to May 31, 2019 in Australia. (a) and (d): Scatter plots between ERA5 IWV against the official Sentinel-3A OLCI IWV and the calibrated Sentinel-3A OLCI IWV for Land group. (b) and (e): Scatter plots between ERA5 IWV against the official Sentinel-3A OLCI IWV and the calibrated Sentinel-3A OLCI IWV for Non-land group. (c) and (f): Scatter plots between ERA5 IWV against the official Sentinel-3A OLCI IWV and the calibrated Sentinel-3A OLCI IWV for all OLCI IWV pixels. All OLCI IWV pixels are obtained from both Land and Non-land groups. N is the number of collocated ERA5-OLCI data points used for comparison analysis. The dashed red lines represent the linear regression of these data. The points coloured with a rainbow scale illustrate the frequency of the OLCI IWV values (brown most frequent, blue least frequent).

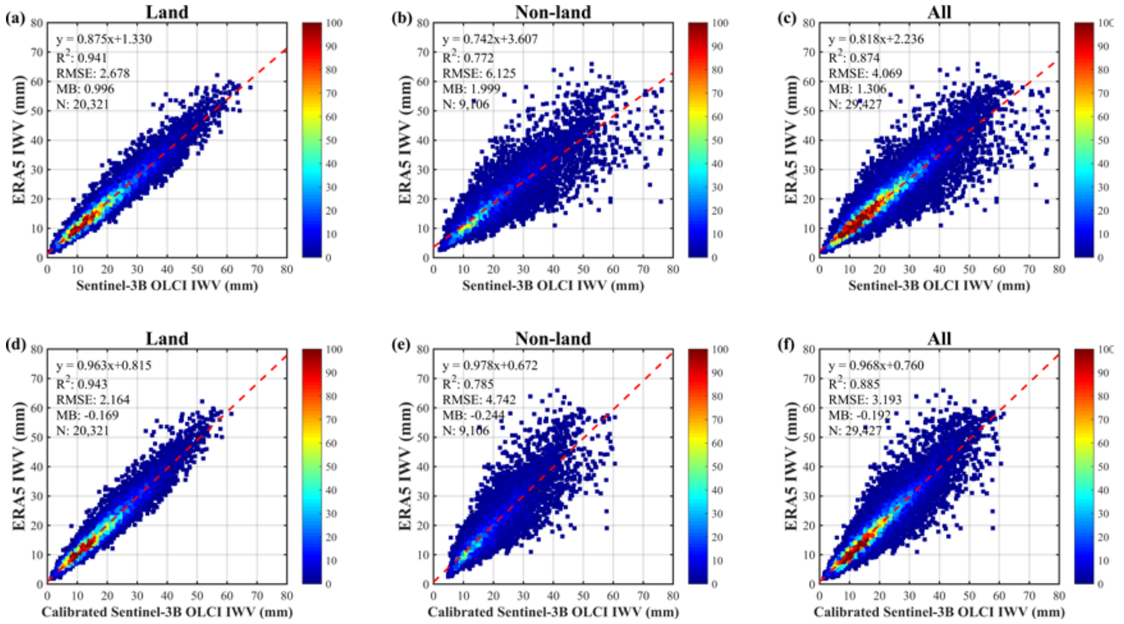

Fig. 9. Comparison of the ERA5 IWV data against the official Sentinel-3B OLCI IWV products (first row) and the calibrated Sentinel-3B OLCI IWV data (second row) from June 1, 2018 to May 31, 2019 in Australia. (a) and (d): Scatter plots between ERA5 IWV against the official Sentinel-3B OLCI IWV and the calibrated Sentinel-3B OLCI IWV for Land group. (b) and (e): Scatter plots between ERA5 IWV against the official Sentinel-3B OLCI IWV and the calibrated Sentinel-3B OLCI IWV for Non-land group. (c) and (f): Scatter plots between ERA5 IWV against the official Sentinel-3B OLCI IWV and the calibrated Sentinel-3B OLCI IWV for all OLCI IWV pixels. All OLCI IWV pixels are obtained from both Land and Non-land groups. N is the number of collocated ERA5-OLCI data points used for comparison analysis. The dashed red lines represent the linear regression of these data. The points coloured with a rainbow scale illustrate the frequency of the OLCI IWV values (brown most frequent, blue least frequent).

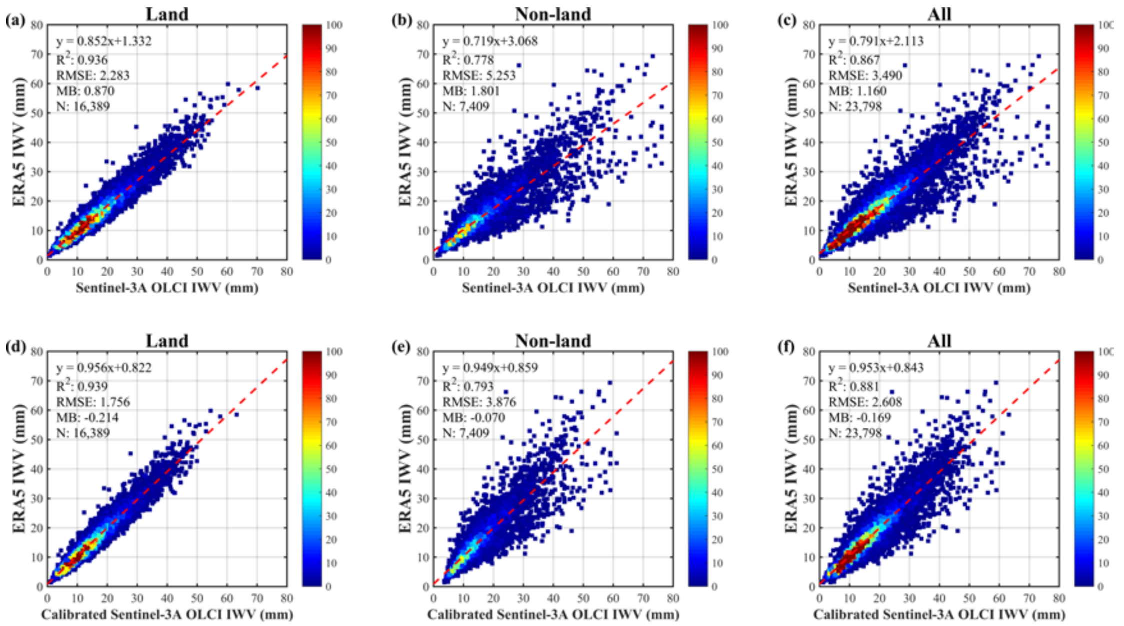

Fig. 10. Comparison of the ERA5 IWV data against the official Sentinel-3A OLCI IWV products (first row) and the calibrated Sentinel-3A OLCI IWV data (second row) from June 1, 2019 to May 31, 2020 in Australia. (a) and (d): Scatter plots between ERA5 IWV against the official Sentinel-3A OLCI IWV and the calibrated Sentinel-3A OLCI IWV for Land group. (b) and (e): Scatter plots between ERA5 IWV against the official Sentinel-3A OLCI IWV and the calibrated Sentinel-3A OLCI IWV for Non-land group. (c) and (f): Scatter plots between ERA5 IWV against the official Sentinel-3A OLCI IWV and the calibrated Sentinel-3A OLCI IWV for all OLCI IWV pixels. All OLCI IWV pixels are obtained from both Land and Non-land groups. N is the number of collocated ERA5-OLCI data points used for comparison analysis. The dashed red lines represent the linear regression of these data. The points coloured with a rainbow scale illustrate the frequency of the OLCI IWV values (brown most frequent, blue least frequent).

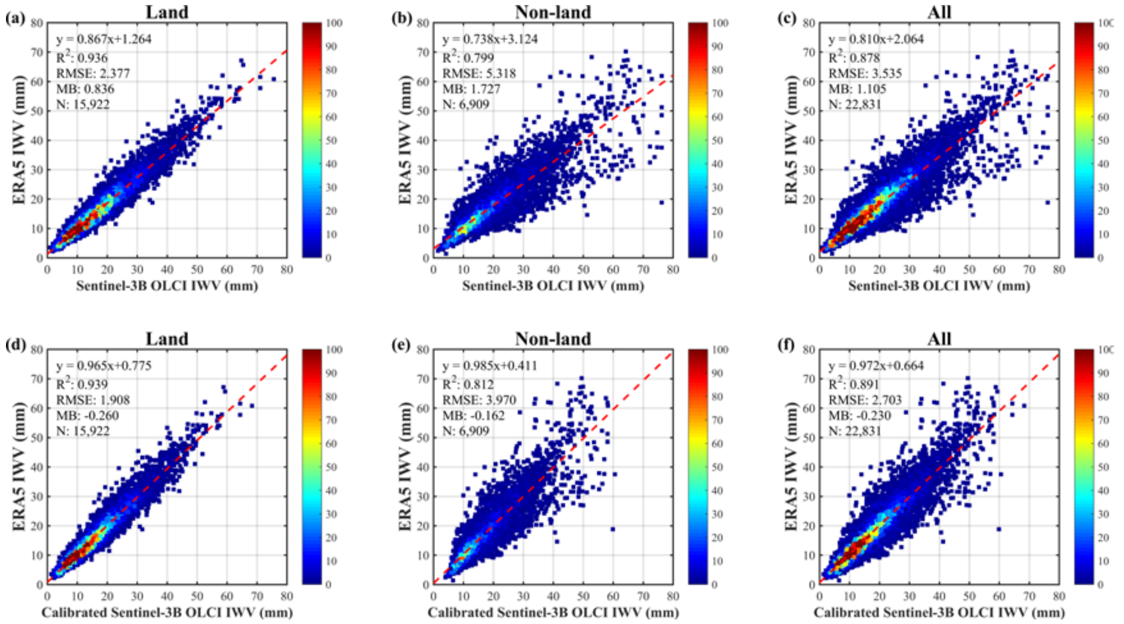

Fig. 11. Comparison of the ERA5 IWV data against the official Sentinel-3B OLCI IWV products (first row) and the calibrated Sentinel-3B OLCI IWV data (second row) from June 1, 2019 to May 31, 2020 in Australia. (a) and (d): Scatter plots between ERA5 IWV against the official Sentinel-3B OLCI IWV and the calibrated Sentinel-3B OLCI IWV for Land group. (b) and (e): Scatter plots between ERA5 IWV against the official Sentinel-3B OLCI IWV and the calibrated Sentinel-3B OLCI IWV for Non-land group. (c) and (f): Scatter plots between ERA5 IWV against the official Sentinel-3B OLCI IWV and the calibrated Sentinel-3B OLCI IWV for all OLCI IWV pixels. All OLCI IWV pixels are obtained from both Land and Non-land groups. N is the number of collocated ERA5-OLCI data points used for comparison analysis. The dashed red lines represent the linear regression of these data. The points coloured with a rainbow scale illustrate the frequency of the OLCI IWV values (brown most frequent, blue least frequent).

TABLE III THE SEASONAL EVALUATION AGAINST REFERENCE ERA5 IWV DATA DURING THE PERIOD BETWEEN JUNE 1, 2018 TO MAY 31, 2020 OVER AUSTRALIA. ALL OLCI IWV PIXELS OBTAINED FROM BOTH LAND AND NON-LAND GROUPS WERE USED

Time span		OLCI product	Sentinel-3A					Sentinel-3B				
			Slope	Intercept	R^2	RMSE	MB	Slope	Intercept	R^2	RMSE	MB
June 1, 2018 to May 31, 2019	Spring	OLCI L2 IWV	0.814	2.179	0.878	3.509	0.889	0.799	2.408	0.861	3.486	0.872
		Calibrated OLCI IWV	0.959	0.895	0.883	2.866	-0.273	0.956	0.912	0.871	2.786	-0.243
	Summer	OLCI L2 IWV	0.804	3.104	0.862	4.402	1.712	0.797	3.602	0.839	4.638	1.601
		Calibrated OLCI IWV	0.980	0.393	0.867	3.410	0.060	0.969	0.652	0.845	3.706	0.085
	Autumn	OLCI L2 IWV	0.796	2.409	0.875	4.339	1.784	0.798	2.341	0.853	4.456	1.676
		Calibrated OLCI IWV	0.973	0.816	0.883	3.200	-0.313	0.980	0.724	0.861	3.450	-0.372
	Winter	OLCI L2 IWV	0.722	2.420	0.814	2.815	0.973	0.713	2.626	0.799	2.947	0.908
		Calibrated OLCI IWV	0.977	0.625	0.842	1.936	-0.373	0.977	0.586	0.833	2.021	-0.328
June 1, 2019 to May 31, 2020	Spring	OLCI L2 IWV	0.817	2.105	0.868	2.744	0.376	0.793	2.373	0.867	2.902	0.472
		Calibrated OLCI IWV	0.953	0.963	0.876	2.328	-0.357	0.942	1.001	0.876	2.340	-0.244
	Summer	OLCI L2 IWV	0.830	2.497	0.894	4.152	1.099	0.788	3.780	0.865	3.974	0.998
		Calibrated OLCI IWV	1.013	-0.273	0.893	3.471	0.005	0.966	0.746	0.868	3.153	-0.015
	Autumn	OLCI L2 IWV	0.758	2.733	0.826	4.388	1.944	0.795	2.281	0.854	4.175	1.695
		Calibrated OLCI IWV	0.935	1.062	0.838	3.161	0.073	0.979	0.628	0.862	3.163	-0.255
	Winter	OLCI L2 IWV	0.736	2.154	0.845	2.710	1.044	0.755	2.102	0.841	2.810	0.945
		Calibrated OLCI IWV	0.973	0.594	0.868	1.797	-0.304	0.984	0.486	0.861	2.006	-0.302

C. *Comparison of GPS IWV Data versus OLCI IWV Products in Mainland China*

To investigate the performance of the developed model on improving Sentinel-3 OLCI IWV products in different regions, evaluation of the calibrated OLCI IWV data against ground-based IWV data from 214 GPS stations is further implemented in Mainland China. The calibrated OLCI IWV data between June 1, 2019 and May 31, 2020 over Mainland China was calculated using the seasonal regression coefficients from the training dataset from June 1, 2018 to May 31, 2019 in Australia. Usually, the season in Australia and Mainland China is exactly opposite, namely, the summer in Australia is the winter in Mainland China. In this comparison analysis, the corresponding matched seasonal-regression-coefficients between Australia and Mainland China was employed to calibrate the Sentinel-3 OLCI IWV products in Mainland China.

As displayed in Fig. 12, the original and the calibrated Sentinel-3A OLCI IWV products were compared against the in-situ GPS-derived IWV data from June 1, 2019 to May 31, 2020 over Mainland China. It is clearly observed that the difference between OLCI IWV products and GPS-derived IWV data was reduced after applying the calibrated model developed in this research. The RMSE between Sentinel-3A OLCI IWV products and GPS IWV observations decreased from 3.026 to 2.701 mm with a reduction of 10.74% for Land group, from 4.969 to 4.010 mm with a reduction of 19.30% for Non-land group, and from 3.947 to 3.306 mm with a reduction of 16.24% for all OLCI IWV pixels, respectively. The slopes of the linear regression lines between them showed a tendency being closer to 1 by comparing with the official Sentinel-3A OLCI IWV products. The MB values were overall positive (overestimated), except for the calibrated Sentinel-3A OLCI IWV products in Land group. In Fig. 13, comparison of the official and the calibrated Sentinel-3B OLCI IWV products against in-situ IWV data from 214 GPS sites from June 1, 2019 to May 31, 2020 over Mainland China is presented. The evaluation results in Fig. 13 show that there was large improvement for the original Sentinel-3B OLCI IWV products when the developed model was applied. For RMSE, it has reduced 12.06% from 3.128 to 2.734 mm for Land group, 22.68% from 5.173 to 4.000 mm for Non-land group, and 18.83% from 4.042 to 3.281 mm for all IWV pixels, respectively. For the linear regression slopes, they tended to be more approximate to 1 after the model calibration. For MB, it was overall positive values (overestimated), except for the calibrated Sentinel-3B OLCI IWV products in Land group. Consequently, the improvement of Sentinel-3 OLCI IWV products observed in Figs. 12 and 13 is further confirmed in Mainland China, implying the effectiveness of the calibrated model developed in this research.

In addition, the seasonal comparison analysis between the calibrated Sentinel-3 OLCI IWV products against the reference GPS-derived IWV data from June 1, 2019 to May 31, 2020 over Mainland China was also performed, with seasonal evaluation results displayed in Table IV. For Sentinel-3A OLCI IWV product, the RMSE has reduced 11.50% from 3.253 to 2.879 mm in spring, and 16.77% from 4.842 to 4.030 mm in summer, 20.86% from 5.005 to 3.961 mm in autumn, and 17.29% from 3.302 to 2.731 mm in winter. For Sentinel-3B OLCI IWV product, the RMSE has reduced 11.28% from 3.184 to 2.825 mm, 18.89% from 5.155 to 4.181 mm, 27.47% from 5.210 to 3.779 mm, and 20.78% from 3.378 to 2.676 mm, respectively. The seasonal slopes for Sentinel-3 satellites were overall closer to 1, after applying the calibrated model developed in this research. The seasonal MB values for Sentinel-3 satellites were greatly reduced after calibration.

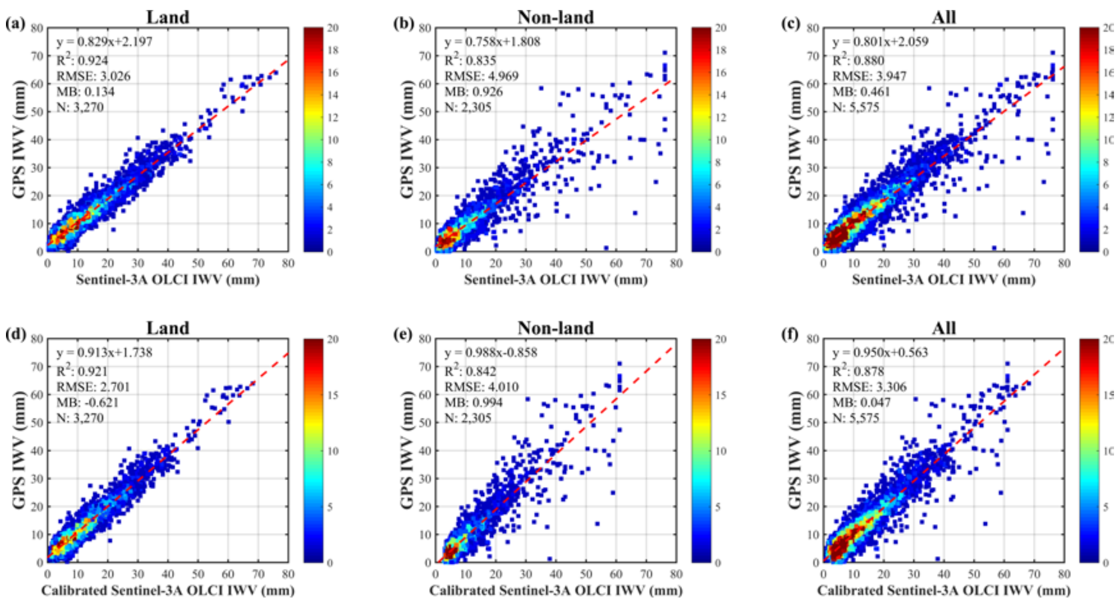

Fig. 12. Comparison of the ground-based GPS-derived IWV data against the official Sentinel-3A OLCI IWV products (first row) and the calibrated Sentinel-3A OLCI IWV data (second row) from June 1, 2019 to May 31, 2020 in Mainland China. (a) and (d): Scatter plots between GPS IWV against the official Sentinel-3A

OLCI IWV and the calibrated Sentinel-3A OLCI IWV for Land group. (b) and (e): Scatter plots between GPS IWV against the official Sentinel-3A OLCI IWV and the calibrated Sentinel-3A OLCI IWV for Non-land group. (c) and (f): Scatter plots between GPS IWV against the official Sentinel-3A OLCI IWV and the calibrated Sentinel-3A OLCI IWV for all OLCI IWV pixels. All OLCI IWV pixels are obtained from both Land and Non-land groups. N is the number of collocated GPS-OLCI data points used for comparison analysis. The dashed red lines represent the linear regression of these data. The points coloured with a rainbow scale illustrate the frequency of the OLCI IWV values (brown most frequent, blue least frequent).

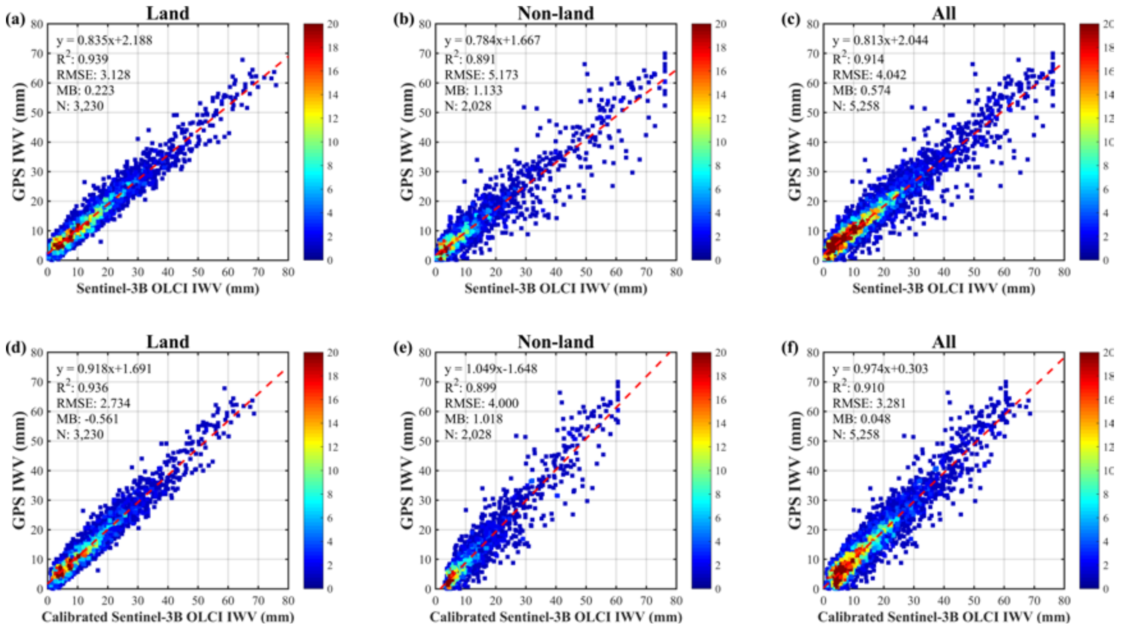

Fig. 13. Comparison of the ground-based GPS-derived IWV data against the official Sentinel-3B OLCI IWV products (first row) and the calibrated Sentinel-3B OLCI IWV data (second row) from June 1, 2019 to May 31, 2020 in Mainland China. (a) and (d): Scatter plots between GPS IWV against the official Sentinel-3B OLCI IWV and the calibrated Sentinel-3B OLCI IWV for Land group. (b) and (e): Scatter plots between GPS IWV against the official Sentinel-3B OLCI IWV and the calibrated Sentinel-3B OLCI IWV for Non-land group. (c) and (f): Scatter plots between GPS IWV against the official Sentinel-3B OLCI IWV and the calibrated Sentinel-3B OLCI IWV for all OLCI IWV pixels. All OLCI IWV pixels are obtained from both Land and Non-land groups. N is the number of collocated GPS-OLCI data points used for comparison analysis. The dashed red lines represent the linear regression of these data. The points coloured with a rainbow scale illustrate the frequency of the OLCI IWV values (brown most frequent, blue least frequent).

TABLE IV The Seasonal Evaluation Against Reference GPS-retrieved IWV data During the Period Between June 1, 2019 to May 31, 2020 over Mainland China. All OLCI IWV Pixels Obtained from Both Land and Non-land Groups Were Used

Time span		OLCI product	Sentinel-3A					Sentinel-3B				
			Slope	Intercept	R^2	RMSE	MB	Slope	Intercept	R^2	RMSE	MB
June 1, 2019 to May 31, 2020	Spring	OLCI L2 IWV	0.795	2.115	0.858	3.253	0.016	0.808	1.972	0.873	3.184	0.019
		Calibrated OLCI IWV	0.918	0.951	0.851	2.879	-0.109	0.955	0.480	0.863	2.825	-0.017
	Summer	OLCI L2 IWV	0.838	1.590	0.904	4.842	1.896	0.840	1.711	0.931	5.155	2.341
		Calibrated OLCI IWV	1.033	-1.62	0.900	4.030	0.945	1.037	-1.843	0.921	4.181	0.958
	Autumn	OLCI L2 IWV	0.749	2.995	0.824	5.005	0.935	0.744	3.518	0.864	5.210	0.866
		Calibrated OLCI IWV	0.926	1.329	0.831	3.961	-0.256	0.940	1.637	0.879	3.779	-0.705
	Winter	OLCI L2 IWV	0.642	2.571	0.605	3.302	-0.295	0.656	2.695	0.712	3.378	-0.224
		Calibrated OLCI IWV	0.899	0.710	0.606	2.731	-0.046	0.947	0.415	0.698	2.676	-0.022

V. Conclusion

The high-accuracy estimation of atmospheric water vapor from satellite instruments is essential to understand the Earth's weather and climate. In this paper, we have developed a calibrated model to improve the accuracy of the official OLCI IWV products published by Sentinel-3 satellites. The model is based on the empirical regression function derived from the differential water vapor information and the official OLCI IWV products, where the differential IWV is estimated from the official OLCI IWV products and ground-based GPS-derived IWV data. It provides an effective way to calibrate current Sentinel-3 OLCI IWV products and improve their retrieval accuracy.

The OLCI IWV pixels were divided into two categories according to the quality flag of each pixel. For each group, the official Sentinel-3 OLCI IWV products and IWV data from 453 GPS stations, from June 1, 2018 to May 31, 2019 over Australia, were utilized as the training datasets to define the regression relationship between the differential IWV and the official OLCI IWV products. When the empirical regression equations were obtained, we calculated the regression parameters from each season for each group. The calculated seasonal empirical regression coefficients were applied to calibrate the official Sentinel-3 OLCI IWV products over Australia and Mainland China. The performance of the calibrated Sentinel-3 OLCI IWV products was evaluated by reference IWV data from ground-based GPS measurements and ECMWF reanalysis products. A total of 453 GPS sites in Australia and 214 GPS sites in Mainland China were selected in this evaluation analysis. Our findings from this study are summarized as follows.

1) Comparison of the official OLCI IWV products and the calibrated OLCI IWV data against ground-based GPS IWV data from June 1, 2018 to May 31, 2019 over Australia, shows an RMSE reduction of 23.28 % from 2.496 to 1.915 mm for Land group, 22.69% from 6.020 to 4.654 mm for Non-land group, and 22.86% from 3.959 to 3.054 mm for all OLCI IWV pixels for Sentinel-3A, and an RMSE reduction of 18.37% from 2.679 to 2.187 mm, 22.42 % from 6.151 to 4.772 mm, and 21.19 % from 4.082 to 3.217 mm for Sentinel-3B, respectively. In addition, the validation results against in-situ GPS IWV data from June 1, 2019 to May 31, 2020 over Australia show that the RMSE was reduced by 28.56% from 2.188 to 1.563 mm for Land group, by 27.28% from 5.311 to 3.862 mm for Non-land group, and by 27.73% from 3.475 to 2.515 mm for all OLCI IWV pixels for Sentinel-3A, and it was reduced by 10.79% from 3.354 to 2.992 mm, by 25.50% from 5.267 to 3.924 mm, and by 18.06 % from 4.030 to 3.302 mm for Sentinel-3B, respectively.

2) Comparison between the official OLCI IWV products and the calibrated OLCI IWV data against reanalysis ERA5 IWV data from June 1, 2018 to May 31, 2019 over Australia, shows that the RMSE has reduced 21.05% from 2.594 to 2.048 mm for Land group, 24.12% from 5.859 to 4.446 mm for Non-land group, and 23.18% from 3.926 to 3.016 mm for all OLCI IWV pixels for Sentinel-3A, and it has reduced 19.19% from 2.678 to 2.164 mm, 22.58% from 6.125 to 4.742 mm, and 21.53% from 4.069 to 3.193 mm for Sentinel-3B, respectively. Meanwhile, the evaluation results against reanalysis ERA5 IWV data between June 1, 2019 to May 31, 2020 over Australia show an RMSE reduction of 23.08% from 2.283 to 1.756 mm for Land group, 26.21% from 5.253 to 3.876 mm for Non-land group, and 25.27% from 3.490 to 2.608 mm for all OLCI IWV pixels for Sentinel-3A, and an RMSE reduction of 19.73% from 2.377 to 1.908 mm, 25.35% from 5.318 to 3.970mm, and 23.54% from 3.535 to 2.703 mm for Sentinel-3B, respectively.

3) Assessment of the performance of the developed model on improving OLCI IWV products between June 1, 2019 and May 31, 2020 in Mainland China shows that the RMSE was reduced by 10.74% from 3.026 to 2.701 mm for Land group, by 19.30% from 4.969 to 4.010 mm for Non-land group, and by 16.24% from 3.947 to 3.306 mm for all OLCI IWV pixels for Sentinel-3A, and it was reduced by 12.60% from 3.128 to 2.734 mm, by 22.68% from 5.173 to 4.000 mm, and by 18.83% from 4.042 to 3.281 mm for Sentinel-3B, by comparing with ground-based water vapor data retrieved from 214 GPS stations.

In summary, this empirical regression model can significantly improve the retrieval accuracy of current Sentinel-3 OLCI IWV products, with a smaller RMSE value compared to the original OLCI IWV products. When using this model to calibrate the OLCI IWV products in different regions, it is recommended that the model coefficients be calculated in the corresponding region.

Acknowledgment

The authors are grateful for Sentinel-3 OLCI IWV data provided by the European Space Agency (ESA). The authors also gratefully acknowledge the support by the Geoscience Australia and the Crustal Movement Observation Network of China (CMONOC) for providing ground-based GPS data used in this paper. The authors would also like to thank the European Centre for Medium-Range Weather Forecasts (ECMWF) for providing reanalysis water vapor data.

References

[1] B. J. Soden, R. T. Wetherald, G. L. Stenchikov, and A. Robock, "Global cooling after the eruption of Mount Pinatubo: A test of climate feedback by water vapor," *Science*, vol. 296, no. 5568, pp. 727–730, Apr. 2002.

[2] T. R. Karl and K. E. Trenberth, "Modern global climate change," *Science*, vol. 302, no. 5651, pp. 1719–1723, Dec. 2003.

[3] S. Bojinski, M. Verstraete, T. C. Peterson, C. Richter, A. Simmons, and M. Zemp, "The concept of essential climate variables in support of climate research, applications, and policy,"

Bull. Am. Meteorol. Soc., vol. 95, no. 9, pp. 1431–1443, Sep. 2014.

[4] I. M. Held and B. J. Soden, “Water vapor feedback and global warming,” *Annu. Rev. Energy Environ.*, vol. 25, no. 1, pp. 441–475, Nov. 2000.

[5] B. C. Gao and A. F. Goetz, “Column atmospheric water vapor and vegetation liquid water retrievals from airborne imaging spectrometer data,” *J. Geophys. Res.: Atmos.*, vol. 95, no. D4, pp. 3549–3564, Mar. 1990.

[6] A. Raval and V. Ramanathan, “Observational determination of the greenhouse effect,” *Nature*, vol. 342, no. 6251, pp. 758–761, Mar. 1989.

[7] Z. Li, J. P. Muller, and P. Cross, “Comparison of precipitable water vapor derived from radiosonde, GPS, and Moderate-Resolution Imaging Spectroradiometer measurements,” *J. Geophys. Res.: Atmos.*, vol. 108, no. D20, Oct. 2003.

[8] K. E. Trenberth, J. Fasullo, and L. Smith, “Trends and variability in column-integrated atmospheric water vapor,” *Clim. Dyn.*, vol. 24, no. 7–8, pp. 741–758, Jun. 2005.

[9] Y. S. Bennouna, B. Torres, V. E. Cachorro, J. P. Ortiz de Galisteo, and C. Toledano, “The evaluation of the integrated water vapour annual cycle over the Iberian Peninsula from EOS-MODIS against different ground-based techniques,” *Q. J. R. Meteorol. Soc.*, vol. 139, no. 676, pp. 1935–1956, Oct. 2013.

[10] J. Vaquero-Martínez *et al.*, “Water vapor satellite products in the European Arctic: An inter-comparison against GNSS data,” *Sci. Total Environ.*, vol. 741, p. 140335, Nov. 2020.

[11] T. S. Glickman and W. Zenk, *Glossary of meteorology*. AMS (American Meteorological Society), 2000.

[12] J. M. Dow, R. E. Neilan, and C. Rizos, “The international GNSS service in a changing landscape of global navigation satellite systems,” *J. Geod.*, vol. 83, no. 3–4, pp. 191–198, Mar. 2009.

[13] X. Li *et al.*, “Accuracy and reliability of multi-GNSS real-time precise positioning: GPS, GLONASS, BeiDou, and Galileo,” *J. Geod.*, vol. 89, no. 6, pp. 607–635, Jun. 2015.

[14] B. Y. Chen and Z. Z. Liu, “A comprehensive evaluation and analysis of the performance of multiple tropospheric models in China region,” *IEEE Trans. Geosci. Remote Sens.*, vol. 54, no. 2, pp. 663–678, Feb. 2016.

[15] F. Solheim *et al.*, “Radiometric profiling of temperature, water vapor and cloud liquid water using various inversion methods,” *Radio Sci.*, vol. 33, no. 2, pp. 393–404, Mar-Apr. 1998.

[16] D. D. Turner, S. A. Clough, J. C. Liljegren, E. E. Clothiaux, K. E. Cady-Pereira, and K. L. Gaustad, “Retrieving liquid water path and precipitable water vapor from the Atmospheric Radiation Measurement (ARM) microwave radiometers,” *IEEE Trans. Geosci. Remote Sens.*, vol. 45, no. 11, pp. 3680–3690, Nov. 2007.

[17] R. Ohtani and I. Naito, “Comparisons of GPS-derived precipitable water vapors with radiosonde observations in Japan,” *J. Geophys. Res.: Atmos.*, vol. 105, no. D22, pp. 26917–26929, Nov. 2000.

[18] A. du Piesanie, A. J. M. Piters, I. Aben, H. Schrijver, P. Wang, and S. Noël, “Validation of two independent retrievals of SCIAMACHY water vapour columns using radiosonde data,” *Atmos. Meas. Tech.*, vol. 6, no. 10, pp. 2925–2940, 2013.

[19] B. N. Holben *et al.*, “AERONET—A federated instrument network and data archive for aerosol characterization,” *Remote Sens. Environ.*, vol. 66, no. 1, pp. 1–16, Oct. 1998.

[20] C. Ichoku *et al.*, “Analysis of the performance characteristics of the five-channel Microtops II Sun photometer for measuring aerosol optical thickness and precipitable water vapor,” *J. Geophys. Res.: Atmos.*, vol. 107, no. D13, Jul. 2002.

[21] J. Vaquero-Martínez *et al.*, “Validation of MODIS integrated water vapor product against reference GPS data at the Iberian Peninsula,” *Int. J. Appl. Earth Obs. Geoinf.*, vol. 63, pp. 214–221, Dec. 2017.

[22] J. Vaquero-Martínez *et al.*, “Inter-comparison of integrated water vapor from satellite instruments using reference GPS data at the Iberian Peninsula,” *Remote Sens. Environ.*, vol. 204, pp. 729–740, Jan. 2018.

[23] J. He and Z. Z. Liu, “Comparison of satellite-derived precipitable water vapor through near-infrared remote sensing channels,” *IEEE Trans. Geosci. Remote Sens.*, vol. 57, no. 12, pp. 10252–10262, Dec. 2019.

[24] M. D. King *et al.*, “Cloud and aerosol properties, precipitable water, and profiles of temperature and water vapor from MODIS,” *IEEE Trans. Geosci. Remote Sens.*, vol. 41, no. 2, pp. 442–458, Feb. 2003.

[25] R. Lang, J. E. Williams, W. J. Van Der Zande, and A. N. Maurellis, “Application of the Spectral Structure Parameterization technique: retrieval of total water vapor columns from GOME,” *Atmos. Chem. Phys.*, vol. 3, pp. 145–160, Feb. 2003.

[26] H. Wang, X. Liu, K. Chance, G. González Abad, and C. C. Miller, “Water vapor retrieval from OMI visible spectra,” *Atmos. Meas. Tech.*, vol. 7, no. 6, pp. 1901–1913, 2014.

[27] Y. J. Kaufman and B. C. Gao, “Remote sensing of water vapor in the near IR from EOS/MODIS,” *IEEE Trans. Geosci. Remote Sens.*, vol. 30, no. 5, pp. 871–884, Sep. 1992.

[28] R. Bennartz and J. Fischer, “Retrieval of columnar water vapour over land from backscattered solar radiation using the Medium Resolution Imaging Spectrometer,” *Remote Sens. Environ.*, vol. 78, no. 3, pp. 274–283, Dec. 2001.

[29] "MODIS Atmospheric Profile Retrieval Algorithm Theoretical Basis Document." [Online]. Available: https://modis.gsfc.nasa.gov/data/atbd/atbd_mod07.pdf.
[30] J. A. Sobrino, J. C. Jimenez-Munoz, C. Mattar, and G. Soria, "Evaluation of Terra/MODIS atmospheric profiles product (MOD07) over the Iberian Peninsula: a comparison with radiosonde stations," *Int. J. Digit. Earth*, vol. 8, no. 10, pp. 771–783, 2015.
[31] T. M. Scheve and C. T. Swift, "Profiling atmospheric water vapor with a K-band spectral radiometer," *IEEE Trans. Geosci. Remote Sens.*, vol. 37, no. 3, pp. 1719–1729, May. 1999.
[32] H. Liu *et al.*, "A physical algorithm for precipitable water vapour retrieval over land using passive microwave observations," *Int. J. Remote Sens.*, vol. 41, no. 16, pp. 6288–6306, Aug. 2020.
[33] C. Donlon *et al.*, "The Global Monitoring for Environment and Security (GMES) Sentinel-3 mission," *Remote Sens. Environ.*, vol. 120, pp. 37–57, May. 2012
[34] N. Lamquin, S. Clerc, L. Bourg, and C. Donlon, "OLCI A/B Tandem Phase Analysis, Part 1: Level 1 Homogenisation and Harmonisation," *Remote Sens.*, vol. 12, no. 11, Jan. 2020.
[35] "Retrieval of Total Water Vapour Content from OLCI Measurements." [Online]. Available: https://earth.esa.int/documents/247904/349589/OLCI_L2_ATBD_Water_Vapour.pdf.
[36] D. Schläpfer, C. C. Borel, J. Keller, and K. I. Itten, "Atmospheric precorrected differential absorption technique to retrieve columnar water vapor," *Remote Sens. Environ.*, vol. 65, no. 3, pp. 353–366, Sep. 1998.
[37] "Sentinel-3: ESA's Global Land and Ocean Mission for GMES Operational Services." [Online]. Available: https://sentinels.copernicus.eu/documents/247904/351187/S3_SP-1322_3.pdf.
[38] J. Liu, H. Liang, Z. Sun, and X. Zhou, "Validation of the Moderate-Resolution Imaging Spectroradiometer precipitable water vapor product using measurements from GPS on the Tibetan Plateau," *J. Geophys. Res: Atmos.*, vol. 111, no. D14, Jul. 2006.
[39] Y. Wang *et al.*, "Evaluation of precipitable water vapor from four satellite products and four reanalysis datasets against GPS measurements on the Southern Tibetan Plateau," *J. Clim.*, vol. 30, no. 15, pp. 5699–5713, Aug. 2017.
[40] K. L. Ccoica-Lopez, J. J. Pasapera-Gonzales, and J. C. Jimenez, "Spatio-temporal variability of the precipitable water vapor over Peru through MODIS and ERA-Interim time series," *Atmosphere*, vol. 10, no. 4, Apr. 2019.
[41] C. Dong *et al.*, "An overview of a new Chinese weather satellite Fy-3A," *Bull. Am. Meteorol. Soc.*, vol. 90, no. 10, pp. 1531-+, Oct. 2009.
[42] S. Gong, D. F. T. Hagan, X. Wu, and G. Wang, "Spatio-temporal analysis of precipitable water vapour over northwest china utilizing MERSI/FY-3A products," *Int. J. Remote Sens.*, vol. 39, no. 10, pp. 3094–3110, 2018.
[43] B. Abbasi *et al.*, "An algorithm to retrieve total precipitable water vapor in the atmosphere from FengYun 3D Medium Resolution Spectral Imager 2 (FY-3D MERSI-2) data," *Remote Sens.*, vol. 12, no. 21, Nov. 2020.
[44] S. Mertikas, P. Partsinevelos, A. Tripolitsiotis, C. Kokolakis, G. Petrakis, and X. Frantzis, "Validation of Sentinel-3 OLCI integrated water vapor products using regional GNSS measurements in Crete, Greece," *Remote Sens.*, vol. 12, no. 16, Jan. 2020.
[45] C. Pigram, "Geoscience Australia – A multi disciplined agency," *Episodes J. Int. Geosci.*, vol. 35, no. 4, pp. 524–525, Dec. 2012.
[46] Q. Chen, S. Song, S. Heise, Y.-A. Liou, W. Zhu, and J. Zhao, "Assessment of ZTD derived from ECMWF/NCEP data with GPS ZTD over China," *GPS Solut.*, vol. 15, no. 4, pp. 415–425, Oct. 2011.
[47] L. Hoffmann *et al.*, "From ERA-Interim to ERA5: The considerable impact of ECMWF's next-generation reanalysis on Lagrangian transport simulations," *Atmos. Chem. Phys.*, vol. 19, pp. 3097–3124, Mar. 2019.
[48] H. Hersbach *et al.*, "The ERA5 global reanalysis," *Q. J. R. Meteorol. Soc.*, vol. 146, no. 730, pp. 1999–2049, Jul. 2020.
[49] M. Bevis, S. Businger, T. A. Herring, C. Rocken, R. A. Anthes, and R. H. Ware, "GPS meteorology: Remote sensing of atmospheric water vapor using the global positioning system," *J. Geophys. Res.: Atmos.*, vol. 97, no. D14, pp. 15787–15801, Oct. 1992.
[50] T. Ning *et al.*, "The uncertainty of the atmospheric integrated water vapour estimated from GNSS observations," *Atmos. Meas. Tech.*, vol. 9, no. 1, pp. 79–92, Jan. 2016.
[51] X. Wang, K. Zhang, S. Wu, S. Fan, and Y. Cheng, "Water vapor-weighted mean temperature and its impact on the determination of precipitable water vapor and its linear trend," *J. Geophys. Res.: Atmos.*, vol. 121, no. 2, pp. 833–852, Jan. 2016.

AUTHORS

Jiafei Xu received the B.Sc. degree in remote sensing science and technology from Shandong Agricultural University, Taian, China, in 2015, and M.Sc. degree in geomatics engineering from Aerospace Information Research Institute, Chinese Academy of Sciences (CAS), Beijing, China, in 2019. He is currently pursuing the Ph.D. degree with the

Department of Land Surveying and Geo-Informatics, The Hong Kong Polytechnic University, Hong Kong.

His current research interests include the algorithm development for precipitable water vapor retrieval from multi-sensor data using ground-based GNSS measurements, and the algorithm validation for various space-sensed precipitable water vapor products by conducting comparisons with reference data, such as GNSS, radiometer, and reanalysis products.

Zhizhao Liu currently is a Professor with the Department of Land Surveying and Geo-Informatics, The Hong Kong Polytechnic University, Kowloon, Hong Kong, China. He earned a B.Sc. degree in Surveying Engineering from Jiangxi University of Science and Technology, Ganzhou, China, in 1994; a M.Sc. degree in Geodesy from the Wuhan University, Wuhan, China, in 1997; and a Ph.D. degree in Geomatics Engineering from the University of Calgary, Calgary, Alberta, Canada, in 2004. His research interests include new algorithm development for precise Global Navigation Satellite System (GNSS), GNSS precise point positioning (PPP), ionosphere modeling and scintillation monitoring, tropospheric remote sensing and modeling, and GNSS meteorology.